PAPER

Check for updates

Modulating oxygen vacancy concentration on $Bi_4V_2O_{11}$ nanorods for synergistic photo-driven plastic waste oxidation and CO_2 reduction†

Mengping Liu,‡[a] Yu Xia,‡[a] Wen Zhao,[a] Ruiyi Jiang,[a] Xin Fu,[a] Brittney Zimmerle,[b] Lihong Tian*[a] and Xiaobo Chen ⓘ *[b]

Sunlight-driven CO_2 reduction coupled with photo-oxidation of plastic waste into value-added chemicals is a very attractive approach towards solving the greenhouse and environmental crisis. Herein, $Bi_4V_2O_{11}$ nanorods with regulable O-vacancy concentration have been synthesized by the solvothermal method, aiming to provide abundant active sites for CO_2 adsorption and boost the separation of photogenerated carriers. In a dual-function system, gas production (CO) mainly from the CO_2 reduction-half-reaction reaches 64.7 $\mu mol\ g^{-1}\ h^{-1}$ on $Bi_4V_2O_{11}$ with rich oxygen vacancies (V_O-BVO-15) in PET hydrolysis solution under 300 W Xe lamp irradiation, 24.5-fold higher than that in 2 M KOH solution. Moreover, a considerable amount of HCOOH product with a conversion rate of 0.7 $mmol\ g_{cata.}^{-1}$ is also achieved under 5 h of irradiation. Glyoxal (6.9 $mmol\ g_{cata.}^{-1}$) and glyoxylate (3.2 $mmol\ g_{cata.}^{-1}$) are produced mainly from the PET oxidation-half-reaction. This work presents an in-depth study of the development of Bi–O–V photocatalysts through defect engineering for photocatalytic CO_2 reduction and demonstrates a promising strategy for reuse of plastic waste and realizing carbon cycle with low energy consumption.

Introduction

Photocatalytic carbon dioxide (CO_2) reduction to obtain hydrocarbon solar fuels is one of the promising strategies to solve the energy crisis and complement carbon cycle.[1,2] The construction of novel semiconductor photocatalysts with excellent photocatalytic activity and high stability has been regarded as one of the best strategies to solve the environmental and energy issues. To date, numerous novel semiconductor photocatalysts such as Bi-, W-, and Mo-containing photocatalysts have been designed and fabricated to solve the problems of traditional photocatalysts. In particular, Bi-containing photocatalysts have been widely investigated in photocatalytic applications because of their outstanding electronic and optical properties.

As one of the important Bi-containing compounds, $Bi_4V_2O_{11}$ has aroused considerable interest owing to its special lamellar structure and good light response. To date, numerous efforts have been made to improve its photocatalytic activity through the fabrication of structures with special morphologies and particle sizes.[3–6] However, the structure and morphology have limited influence on its photocatalytic performance. Despite considerable efforts, the practical application of $Bi_4V_2O_{11}$ in photocatalysis is still suppressed because of the low light absorption, high recombination rate of photoinduced charge pairs and inadequate surface reactive sites in pristine $Bi_4V_2O_{11}$.

Oxygen vacancies (V_Os) are of particular interest for the enhanced adsorption and activation of inert gas molecules and guiding chemical reactions through more efficient pathways that lower the energy barrier.[7] Depending on the coverage and adsorption geometry, O_2, CO_2, and N_2 are activated to their high-energy intermediates.[8] The concept of V_Os was firstly proposed by Tompkins *et al.* in the 1960s, where V_Os were considered as a kind of species.[9] Because of the special synthetic conditions and unstable surface structure of photocatalysts, O atoms are prone to move into random positions or even burst out of the crystal lattice.[10] In general, V_Os are more easily generated by high temperature and/or pressure, chemical reduction, ion doping or light irradiation, which can lead to the bond breaking with lattice distortion and formation of defective states and electronic compensation in photocatalysts, therefore promoting the critical steps in photocatalytic processes. V_Os are recommended to be one of the most important and prevalent anion defects with a relatively lower formation energy on many

[a]*Collaborative Innovation Center for Advanced Organic Chemical Materials Constructed by the Province and Ministry, Ministry of Education Key Laboratory for the Synthesis and Application of Organic Functional Molecules, College of Chemistry and Chemical Engineering, Hubei University, Wuhan 430062, China. E-mail: tian7978@hubu.edu.cn*

[b]*Division of Energy, Matter and Systems, School of Science and Engineering, University of Missouri-Kansas City, Kansas City, USA. E-mail: chenxiaobo@umkc.edu*

† Electronic supplementary information (ESI) available: Fig. S1–S4 and Tables S1, S2. See DOI: https://doi.org/10.1039/d2ta09345f

‡ The authors contributed equally to this work.

oxide surfaces. In this regard, introducing V_Os on photocatalysts could provide a new perspective to optimize the activity of CO_2 photoconversion. Though $Bi_4V_2O_{11}$ is an intrinsic oxygen deficient material, constituted by a $[Bi_2O_2]^{2+}$ layered skeleton spaced by deficient perovskite-like VO_x linkages[11] and the oxygen environment around vanadium is adjustable, which results in the unique structure features of $Bi_4V_2O_{11}$ based compounds,[12–14] few studies focus on investigating the effect of V_Os on photocatalytic CO_2 reduction on $Bi_4V_2O_{11}$.

The control of the oxidation half reaction is the key to promote charge carrier separation.[15] In the research system of photocatalytic reduction of CO_2, a certain amount of hole sacrificial agents, such as triethylamine, triethanolamine, ammonium oxalate, *etc.*, is often added to the reaction, but they are generally expensive and toxic. Plastic is a precious resource that can store a large amount of energy and chemical raw materials, but most of it is simply thrown into landfills, which not only greatly wastes plastic resources, but also causes great damage to the environment.[16] Recently several studies involving photo-reforming of plastics coupled with the photolysis of water to produce hydrogen successfully bring the treatment of waste plastics into the photocatalytic redox system to achieve maximum utilization of energy.[17–20]

Herein, we successfully synthesize $Bi_4V_2O_{11}$ with gradient oxygen vacancies and first attempt to use plastic waste in the dual-function photocatalytic system, in the search for ways to mitigate the greenhouse effect and explore the degradation of plastic waste to alleviate the earth's "plastic crisis". Our experimental results indicate that the PET photo-oxidation and CO_2 photoreduction reinforce each other. In a dual-function system, the plastic pollutant PET is oxidized into some high value-added products, avoiding the use of commonly used expensive and often toxic hole sacrificial agents, thus achieving sustainable reduction of CO_2 to CO and HCOOH. Although this idea is still in the experimental stage, the use of this dual-use technology provides a new pathway to tackle many major environmental challenges such as global warming, and plastic waste.

Experimental

Materials

Ethylene glycol ($C_2H_6O_2$, AR, $\geq$98%), ammonia ($NH_3 H_2O$, AR, 25–28%) and sodium hydroxide (NaOH, AR, $\geq$96%) were purchased from Sinopharm Group. Bismuth nitrate pentahydrate ($Bi(NO_3)_3 \cdot 5H_2O$) and ammonium metavanadate (NH_4VO_3) were supplied by Aladdin-Reagent. All chemical reagents were used without further purification.

Synthesis of defective $Bi_4V_2O_{11}$ nanorods

The typical experimental procedure is as follows: first, 0.34 g urea and 1.30 g $Bi(NO_3)_3 \cdot 5H_2O$ were added to 15.0 mL ethylene glycol (EG) marked as solution A under continuous stirring. Second, 0.156 g NH_4VO_3 was dissolved in another 15.0 mL ethylene glycol (EG) marked as solution B. Solution B was added to solution A under continuous stirring for 30 minutes, and the

pH value of the final system was adjusted to 9.00 using dilute ammonia water at room temperature under constant magnetic stirring. Subsequently, the formed mixture was poured into a stainless-steel autoclave with a Teflon liner of 50 mL capacity and heated at 180 °C for different reaction times (hours). Finally, the reactor was cooled to room temperature naturally. The resulting samples were washed with deionized water and ethanol several times and dried at 80 °C in an oven overnight. The obtained powders were marked as V_O-BVO-t, where t represents the reaction time.

Characterization

The crystal structure of the samples was characterized by employing a Rigaku X-ray diffractometer with a Cu-Kα (λ = 1.540 Å) radiation source in the 2θ range of 10–60°. Raman spectroscopy data were collected using a Renishaw InVia Raman microscope with an excitation wavelength of 532 nm. The morphologies were observed on a high-resolution transmission electron microscope (HRTEM, FEI Tecnai F20). The X-ray photoelectron spectroscopy measurement of materials was carried out on a VG Multilab 2000 spectrometer with an Al Kα X-ray source (Thermo Electron Corporation), and all the spectra were calibrated to the C 1s peak at 284.8 eV. The CO_2 adsorption experiment was performed on a V-Sorb 2800TP volumetric specific surface area and aperture analyzer. All samples were treated at 120 °C in a vacuum to remove trapped gas and humidity. High purity CO_2 directly connects the analyzer. CO_2 adsorption isotherms were determined in the range of 0.01 Pa to 1.8 bar at room temperature. A Micromeritics Autochem II chemisorption analyzer with a thermal conductivity detector was used to conduct CO_2 temperature programmed desorption (CO_2-TPD) on materials. The thermal desorption of chemisorbed CO_2 was performed in flowing He at a ramp rate of 5 °C min^{-1} to a final temperature of 700 °C. Electrochemical measurements were implemented on an electrochemical apparatus (CHI760E, China) in a standard three-electrode system with the as-prepared samples as the working electrode, a Pt wire as the counter electrode and a saturated calomel electrode as the reference electrode. Time-resolved photoluminescence spectra (TRPL) were measured on an FLS980 fluorescence spectrometer (Edinburgh Instruments, UK) with an excitation wavelength of 250 nm.

Substrate pre-treatment

PET powders were added into 1 L KOH aqueous solution, which was incubated at 40 °C with stirring at 480 rpm for 24 h in air to obtain different concentrations of PET hydrolysis solution.[19] After cooling to room temperature, the mixture was centrifuged at 8000 rpm for 3 min, and the supernatant was then extracted for further use.

Photocatalytic reaction

The photocatalytic experiment was conducted in a Pyrex glass reactor with a volume of 400 mL (Beijing Perfectlight Technology Co., Ltd, China). Typically, 25 mg catalyst was dispersed into 50 mL 2 M KOH aqueous solution and then 50 mL pretreated PET solution was added. In order to achieve an

This journal is © The Royal Society of Chemistry 2023

J. Mater. Chem. A, 2023, **11**, 12770–12776 | **12771**

adsorption–desorption balance between the catalyst and the substrate, the system was stirred continuously for 30 min in the dark. Prior to the light irradiation, the above system was vacuum-treated to remove the air completely, and purged with CO_2 (99.999%) with a flow rate of 5 mL min^{-1} for 30 min. After that, the reactor was irradiated from the top using a high-pressure xenon lamp as the light source (CEL-HXF300, Beijing Perfect Light Technology Co., Ltd, China). The reaction was kept at constant temperature by a circulating water system. At the given interval, 1.0 mL of gas was taken from the reaction cell and analysed on a gas chromatograph (GC, Zhejiang Fuli Analytical Instrument Co., Ltd, China) equipped with a flame ionization detector (FID, GDX-01 columns). Liquid products were detected by ^{1}HNMR spectra.

Results and discussion

Characterization of defective $Bi_4V_2O_{11}$

The targeted $Bi_4V_2O_{11}$ is synthesized by the solvothermal method in ethylene glycol solvent, and oxygen vacancy concentration is modulated through controlling the reaction time. As shown in Fig. 1a, all diffraction peaks in powder XRD patterns of V_O-BVO-9, V_O-BVO-12 and V_O-BVO-15 are well indexed to $Bi_4V_2O_{11}$ without any observable impurity. The strongest peak in the magnified patterns (Fig. 1b) is located at about 28.6° in the former two materials, corresponding to orthorhombic $Bi_4V_2O_{11}$ (β-$Bi_4V_2O_{11}$, JCPDS 42-0135). However, this diffraction peak shifts to 28.7° in V_O-BVO-15, indicating a possible phase distortion.[11] When the reaction time exceeds 24 h, a small quantity of $BiVO_4$ impurity is present (marked with an asterisk in Fig. 1a). Raman spectra further provide the fundamental information on the metal–oxygen bond in all as-

prepared $Bi_4V_2O_{11}$ materials. The Bi–O stretching modes are too weak to be accessible in low wavenumber. Raman modes of V–O bonds are visible between 600 and 1000 cm^{-1} (Fig. 1c). Two distinct split peaks at around 840 and 880 cm^{-1} are ascribed to the stretching vibrations of V–O bonds with different bond lengths, monometric V–O tetrahedron and perovskite-like V–O–V bond.[21,22] The weak band at 685 cm^{-1} is related to the doubly coordinated (V–O–V) oxygen atom.[21] It is worth noting that the vibrational bands of V–O–V bonds gradually decrease with prolonged reaction time, while the reverse happens to the VO_4 tetrahedron (840 cm^{-1}); especially, the additional shoulder at about 800 cm^{-1} indicates that the dramatic increase of V^{5+} occupied the perfect VO_4 tetrahedral sites in V_O-BVO-24, probably originating from the $BiVO_4$ impurity.[23] These results illustrate that the crystalline distortion of as-prepared $Bi_4V_2O_{11}$ materials (XRD results) is determined by the structural variation of V–O polyhedra induced by oxygen vacancies.

V 2p and O 1s XPS spectra are recorded to further investigate the surface compositions and chemical interaction with the C 1s level at 284.8 eV as the binding energy (BE) reference. As shown in Fig. 1d, the BE of V 2p$_{3/2}$ is located at ~516.3 eV, much lower than the BE of V^{5+} (~517 eV),[24] suggesting the presence of V_Os in all as-prepared $Bi_4V_2O_{11}$ materials. In fitted O 1s spectra (Fig. 1e), the main peak at 529.3 eV is ascribed to lattice O^{2-} anions in $Bi_4V_2O_{11}$, and two signals at 1.3 and 2.4 eV higher BE of O^{2-} can be assigned to adsorbed –OH and H_2O on metal sites adjacent to V_Os in order to maintain charge balance.[25–27] The corresponding intensity of –OH and H_2O peaks is indirectly proportional to the concentration of oxygen vacancies.[28] Note that the intensity of –OH and H_2O gradually increases initially but dramatically decreases when the reaction time exceeds 24 h, suggesting the concentration of V_Os with the order of V_O-BVO-24
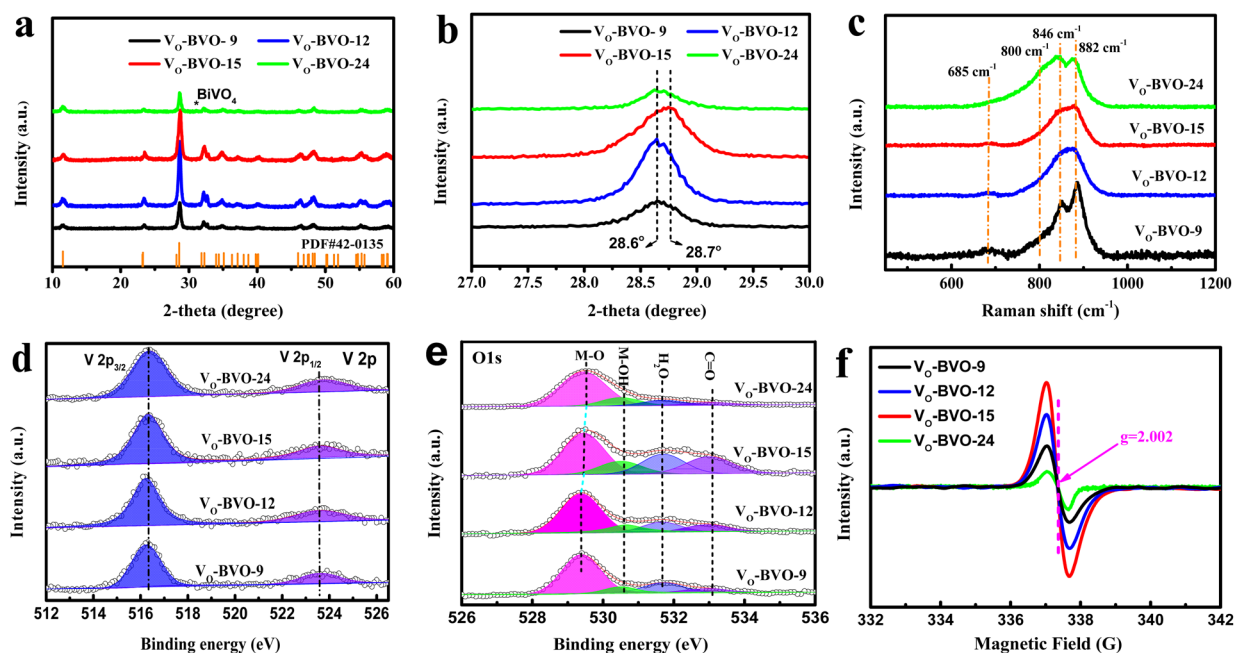

Fig. 1 (a) XRD patterns, (b) the magnified XRD patterns, (c) Raman spectra, (d) V 2p and (e) O 1s XPS spectra, and (f) EPR spectra of V_O-BVO-9, V_O-BVO-12 and V_O-BVO-15.

12772 | J. Mater. Chem. A, 2023, 11, 12770–12776

This journal is © The Royal Society of Chemistry 2023

Fig. 2 (a) TEM image of V_O-BVO-9, V_O-BVO-12 and V_O-BVO-15. (b) HRTEM image of V_O-BVO-15 and selected area electron diffraction graph (the inset).

< V_O-BVO-9 < V_O-BVO-12 < V_O-BVO-15. EPR spectra in Fig. 1f also verify that V_O-BVO-15 possesses the most V_Os because of the strongest signal at $g = 2.002$ originating from the unpaired electrons at oxygen vacancies.[29–31]

Apart from the slight structure distortion, the morphologies of $Bi_4V_2O_{11}$ are also strongly controlled by the concentration of oxygen vacancies. As shown in Fig. 2a, V_O-BVO-9 with less V_Os features irregular nanosheets mixed with seed-like nanorods. With the increase of V_O concentration, these nanosheets gradually develop into long nanorods with a length of about 100–300 nm and width of 20 nm (V_O-BVO-15). V_O-BVO-24 remains a nanorod structure but becomes shorter and wider compared with V_O-BVO-15. The HRTEM graph of V_O-BVO-15 exhibits the lattice fringes with an interplanar spacing of 0.77 nm and 0.28 nm in Fig. 2b, assigned to (002) and (020) crystal facets, respectively. The selected area electron diffraction (SAED) of

nanorods shows well-defined electron diffraction spots and further confirms that the lattice distances of (002) and (020) planes are dominant on nanorods (the inset in Fig. 2b). On the edge of the nanorod, a clear disorder layer is observable due to V_Os.

Photo-driven CO_2 reduction coupled with PET oxidation

The synergistic ox/red reaction of CO_2 and PET on different defective $Bi_4V_2O_{11}$ samples is evaluated in KOH aqueous solution (pH = 14.16) under full-wavelength light irradiation (intensity: 150 mW cm^{-2}). All gas and liquid products are investigated by GC and ^{1}H-NMR spectra in detail. Fig. 3a demonstrates CO_2 reduction on various catalysts in KOH solution (2M) without PET, which is highly related to the oxygen vacancy concentration in catalysts, and the highest CO conversion rate is 2.6 μmol g^{-1} h^{-1} on V_O-BiVO-15 with the most oxygen vacancies. Though the value is far higher than those reported for $Bi_4V_2O_{11}$ composites (<1 μmol g^{-1} h^{-1}),[32] it is still unsatisfactory. An attempt is made to conduct the synergistic catalytic CO_2 reduction and industrial PET oxidation in one system. CO and HCOOH are the main products from CO_2 photoreduction. Fig. 3b compares the conversion rates of CO and HCOOH on V_O-BiVO-15 in the presence of different PET contents. It is found that the synergistic PET oxidation can significantly improve CO_2 reduction, and CO_2-to-CO conversion rate increases to 64.7 μmol g^{-1} h^{-1} at the optimal PET content of 20 g L^{-1}, about 24.5-fold higher than that from the sole CO_2 reduction in KOH solution. ^{1}HNMR spectra of solution before and after photocatalytic reaction are presented in Fig. 3c. The
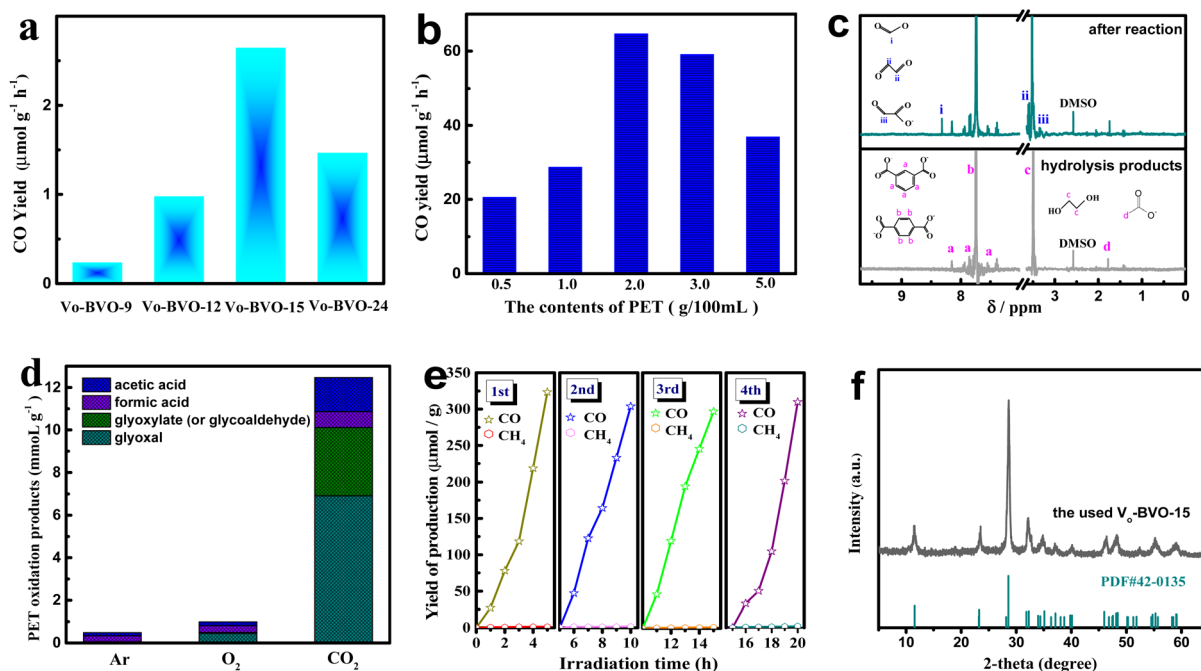

Fig. 3 (a) Photocatalytic CO_2 reduction in 2 M KOH solution using V_O-BVO-t catalysts without PET; (b) CO yield in dual-functional system with different concentrations of PET substrate; (c) ^{1}H-NMR spectra of PET (20 g L^{-1}) hydrolysis products before and after photocatalytic reaction; (d) photocatalytic reaction in different atmosphere with PET (20 g L^{-1}). (e) Gas products from cyclic experiments of photocatalytic CO_2 reduction synergistic PET (20 g L^{-1}) oxidation on V_O-BVO-15. (f) The XRD pattern of the used V_O-BVO-15.

This journal is © The Royal Society of Chemistry 2023

J. Mater. Chem. A, 2023, **11**, 12770–12776 | **12773**

hydrolysis products of industrial PET in KOH solution (before photochemical reaction) are identified to be composed of a large amount of ethylene glycol (EG, c) and a little phthalic acid (a) and acetic acid (d) after removing the insoluble terephthalic acid (TPA, b) by filtration, which could be reused as feedstocks in the synthesis of PET.[20] After photocatalytic reaction, new signals of formic acid (i), glyoxal (ii), and glyoxylate/glycoaldehyde (iii) are visible. Accordingly, the HCOOH (i) product originates from CO_2 reduction with a yield of 0.7 mmol $g_{cata.}^{-1}$ under 5 h of irradiation.

Products (ii) and (iii) are ascribed to the PET oxidation-half-reaction, which are not detected in the absence of light irradiation or catalysts. The CO_2 bubbling consumedly improves the PET oxidation, compared with an Ar or O_2 atmosphere. As shown in Fig. 3d, the production rate reaches 6.9 mmol $g_{cata.}^{-1}$ for glyoxal (ii) and 3.2 mmol $g_{cata.}^{-1}$ for glyoxylate (or glycoaldehyde) (iii), almost 15 and 64 fold those under an O_2 atmosphere, respectively. These results indicate that CO_2 bubbling is highly effective in promoting the selective photo-oxidation of PET components to organic chemicals on V_O-BVO catalysts.

The stability of V_O-BVO-15 in a synergistic reaction of CO_2 reduction and PET oxidation is investigated by quantifying CO product in four cycle experiments with each run for 5 h. Fig. 3e displays that CO evolution yield had no obvious decline in four cycle experiments. The XRD pattern of the used V_O-BVO-15 well corresponds to $Bi_4V_2O_{11}$ without noticeable impurity in Fig. 3f. The used V_O-BVO-15 still retains a similar morphology (nanorods) to the fresh one (Fig. S1†). The above results indicate a good durability of V_O-BiVO-15 in long-term photocatalytic synergistic reaction of CO_2 reduction and PET oxidation.

Role of V_Os in enhanced photocatalytic activity

From the photocatalytic kinetic viewpoint, the adsorption of substrate, *e.g.*, CO_2 on a catalyst is an important prerequisite for product efficiency.[33] Fig. 4a illustrates that the order of CO_2 uptake capacity is V_O-BVO-9 (0.0667 mmol g^{-1}) < V_O-BVO-12 (0.1169 mmol g^{-1}) < V_O-BiVO-15 (0.1603 mmol g^{-1}) at 298 K and 1.8 bar, probably ascribed to the gradually increased surface areas analysed by N_2 adsorption–desorption isotherms (Fig. S2, ESI†). CO_2-TPD measurements are performed to determine the strength distribution of basic sites on all catalysts. Except for the weak physical adsorption for CO_2 in 50–150 °C,[34,35] the strong chemical adsorption appears at 400–600 °C in Fig. 4b. V_O-BiVO-9 with less V_Os only shows a peak at about 420 °C. With the

increase of V_Os, the peak becomes stronger and wider and shifts to higher temperature for V_O-BiVO-12 and V_O-BiVO-15. In addition, a sharp peak at higher temperature between 500 and 600 °C is probably attributed to the formed CO_3^{2-} with Bi^{3+} in the CO_2-TPD spectrum of V_O-BiVO-15.[34,35] The quantity of various basic sites is determined by the integral of peak area and displayed in Table S1.† Obviously, V_O-BiVO-15 possesses the most basic sites for CO_2 adsorption among the three catalysts owing to the highest concentration of V_Os, which are beneficial for CO_2 adsorption and activation.

In addition, UV-Vis DRS spectra present gradually enhanced light absorption from V_O-BVO-9 to V_O-BVO-15 due to the increase of V_O concentration (Fig. 5a),[36,37] in accordance with the colour change from yellowish-green to yellowish-brown (the inset in Fig. 5a). Moreover, a bump correlative to the V_O-induced defect state becomes more obvious between 600 and 700 nm,[32,38] which probably forms an intermediate energy level for charge transfer. The corresponding optical band gap is determined by the Kubelka–Munk formula to be 2.48 eV (V_O-BVO-9), 2.41 eV (V_O-BVO-12) and 2.36 eV (V_O-BVO-15), respectively (inset in Fig. 5a).[30] XPS valence spectra demonstrate an almost similar valence band maximum (VBM) at 1.67 eV for the three samples (Fig. S3, ESI†). As a result, the conduction band minimum (CBM) calculated according to $E_{CB} = E_{VB} - E_g$ exhibits a slight positive-shift due to gradually narrowed band gap, *i.e.*, −0.81 eV for V_O-BVO-9, −0.74 eV for V_O-BVO-12 and −0.69 eV for V_O-BVO-15, as shown in Fig. 5b, which are sufficient for CO_2 reduction to CO and HCOOH.

To confirm V_Os promoting charge carrier migration, electrochemical experiments including photocurrent response and EIS spectra are performed. Fig. S4 in the ESI† demonstrates the stable and reproducible on-off current on all samples with/without light irradiation. The photocurrent density on V_O-BVO-15 is about 1.31 and 1.62 times that of V_O-BVO-12 and V_O-BVO-9, respectively, indicating the fastest photogenerated
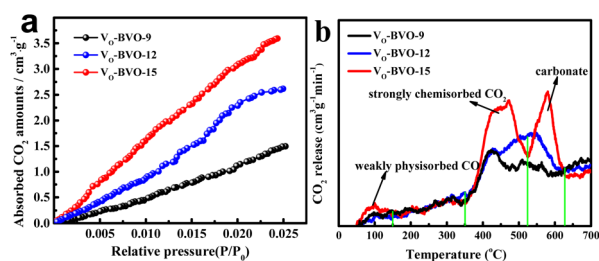

Fig. 5 UV-Vis spectra and $(\alpha h\nu)^2$ functions as $h\nu$ curves (a), schematic diagram of the energy band structure (b), electrochemical impedance spectra (c) and TRPL spectra (d) of V_O-BVO-9, V_O-BVO-12 and V_O-BVO-15.

Fig. 4 (a) CO_2 absorption–desorption isotherms and (b) CO_2-TPD curves of V_O-BVO-9, V_O-BVO-12 and V_O-BVO-15.

12774 | *J. Mater. Chem. A*, 2023, **11**, 12770–12776

This journal is © The Royal Society of Chemistry 2023

electron transfer on V_O-BVO-15. In electrochemical impedance spectra (EIS) (Fig. 5c), the semicircle radius in the high frequency region diminishes with the increase of V_O concentration on the catalyst, which also elucidates the decreasing electron transfer resistance on the electrode interface with increasing V_Os.[39]

The TRPL spectra are studied to further understand the charge transfer process. The collected spectra are displayed in Fig. 5d, and the PL decay lifetime (τ) components and corresponding intensity (A) are extracted by curve fitting using a two-exponential function and shown in Table S2.†[40] Both short lifetime τ_1 and long lifetime τ_2, related to intrinsic fluorescence from radiative decay and non-radiative coupling, respectively, prolong with the increase of oxygen vacancy concentration. The resultant average lifetime ($\tau_{av.}$) gradually increased, *i.e.*, 4.1 ns for V_O-BVO-9 < 6.5 ns for V_O-BVO-12 < 16.1 ns for V_O-BVO-15, indicating that oxygen vacancies effectively promote charge carrier separation; especially, non-radiative recombination related to defects is dramatically suppressed due to the intensity (A_2) drop from 16% on V_O-BVO-9 to 6.5% on V_O-BVO-15. This is presumedly associated with the special $Bi_4V_2O_{11}$ structure that V_Os generally reside in V–O layers ($\langle 110 \rangle$ direction).[41] The increase of V_O concentration greatly improves the oxygen ion migration in $Bi_4V_2O_{11}$, thus enhancing the conductivity (electrochemical results) and decreasing non-radiative recombination.

Conclusions

In this work, for the first time, $Bi_4V_2O_{11}$ photocatalysts with modulating V_Os are used in a dual-functional system to photocatalyse carbon dioxide reduction and plastic waste oxidation. V_Os significantly promote the light adsorption, and charge separation and provide abundant sites for CO_2 capture, thus synergistically improving the photocatalytic CO_2 reduction and PET oxidation. In a dual-function system, CO_2-to-CO conversion rate increases to 64.7 μmol g^{-1} h^{-1} at the optimal PET content of 20 g L^{-1}, about 24.5-fold higher than that from the sole CO_2 reduction in KOH solution. Despite this, a considerable amount of HCOOH is also produced with a yield of 0.7 mmol $g_{cata.}^{-1}$ under 5 h of irradiation. In the oxidation-half-reaction, considerable glyoxal and glyoxylate are produced by oxidation of glycol coming from PET hydrolysis. As a result, this study provides a novel strategy to reuse plastic waste and promote carbon cycle with low energy consumption.

Conflicts of interest

There are no conflicts to declare.

Acknowledgements

Notes and references

1 L. Yi, W. Zhao, Y. Huang, X. Wu, J. Wang and G. Zhang, *Sci. China Mater.*, 2020, **63**, 2206–2214.

2 L. Jiang, K. Wang, X. Wu and G. Zhang, *Sol. RRL*, 2021, **5**, 2000326.

3 T. Liu, Y. G. Mao and Y. Peng, *CrystEngComm*, 2018, **20**, 2553.

4 M. Liang, L. Chen, Z. Yang, Z. Zeng and S. Yang, *Funct. Mater. Lett.*, 2019, **12**, 1850109.

5 Y. Lin, H. Cai, H. Chen and H. Luo, *Appl. Surf. Sci.*, 2021, **544**, 148921.

6 L. Zong, P. Cui, F. Qin, K. Zhao, Z. Wang and R. Yu, *Mater. Res. Bull.*, 2017, **86**, 44–50.

7 J. Li, H. Li, G. Zhan and L. Zhang, *Acc. Chem. Res.*, 2017, **50**, 112–121.

8 H. Li, J. Shang, Z. Ai and L. Zhang, *J. Am. Chem. Soc.*, 2015, **137**, 6393–6399.

9 F. C. Tompkins, *Nature*, 1960, **186**, 3–6.

10 L. Hao, H. Huang, Y. Zhang and T. Ma, *Adv. Funct. Mater.*, 2021, **31**, 2100919.

11 C. Lv, G. Chen, J. Sun and Y. Zhou, *Inorg. Chem.*, 2016, **55**, 4782–4789.

12 G. Mairesse, P. Roussel, R. N. Vannier, M. Anne and G. Nowogrocki, *Solid State Sci.*, 2003, **5**, 861–869.

13 Y. Zhang and Y. Ueda, *Inorg. Chem.*, 2013, **52**, 5206–5213.

14 Y. Zhang, T. Yamamoto, M. A. Green, H. Kageyama and Y. Ueda, *Inorg. Chem.*, 2015, **54**, 10925–10933.

15 H. Liu, C. Xu, D. Li and H. L. Jiang, *Angew. Chem., Int. Ed.*, 2018, **130**, 5477–5481.

16 J. R. Jambeck, R. Geyer, C. Wilcox, T. R. Siegler, M. Perryman, A. Andrady, R. Narayan and K. L. Law, *Science*, 2015, **347**, 768–771.

17 M. F Kuehnel and E. Reisner, *Angew. Chem., Int. Ed.*, 2018, **57**, 3290–3296.

18 Y. Li, S. Wan, C. Lin, Y. Gao, Y. Lu, L. Wang and K. Zhang, *Sol. RRL*, 2021, **5**, 2000427.

19 T. Uekert, M. F. Kuehnel, D. W. Wakerley and E. Reisner, *Energy Environ. Sci.*, 2018, **111**, 2853–2857.

20 T. Uekert, H. Kasap and E. Reisner, *J. Am. Chem. Soc.*, 2019, **141**, 15201–15210.

21 A. K. Arora, T. Sato, T. Okada and T. Yagi, *Phys. Rev. B: Condens. Matter Mater. Phys.*, 2012, **85**, 094113.

22 K. Trzciński, J. Gasiorowski, A. B. Centkowska, M. Szkoda, M. Sawczak, K. Hingerl, D. R. T. Zahn and A. L. Oleksiak, *Thin Solid Films*, 2017, **638**, 251–257.

23 F. D. Hardcastle and I. E. Wachs, *J. Solid State Chem.*, 1991, **90**, 194–210.

24 G. Silversmit, D. Depla, H. Poelman, G. B. Marin and R. D. Gryse, *J. Electron Spectrosc. Relat. Phenom.*, 2004, **135**, 167–175.

25 C. Lv, G. Chen, X. Zhou, C. Zhang, Z. Wang, B. Zhao and D. Li, *ACS Appl. Mater. Interfaces*, 2017, **9**, 23748–23755.

26 H. L. Tan, A. Suyanto, A. T. D. Denko, W. H. Saputera, R. Amal, F. E. Osterloh and Y. H. Ng, *Part. Part. Syst. Charact.*, 2017, **34**, 1600290.

This journal is © The Royal Society of Chemistry 2023

J. Mater. Chem. A, 2023, **11**, 12770–12776 | **12775**

27 H. Ali-Löytty, M. W. Louie, M. R. Singh, L. Li, H. G. S. Casalongue, H. Ogasawara, E. J. Crumlin, Z. Liu, A. T. Bell, A. Nilsson and D. Friebel, *J. Phys. Chem. C*, 2016, **120**, 2247–2253.

28 W. C. Huo, X. Dong, J. Y. Li, M. Liu, X. Y. Liu, Y. X. Zhang and F. Dong, *Chem. Eng. J.*, 2019, **361**, 129–138.

29 X. Y. Kong, Y. Y. Choo, S. P. Chai, A. K. Soh and A. R. Mohamed, *Chem. Commun.*, 2016, **52**, 14242–14245.

30 Y. Lv, W. Yao, R. Zong and Y. Zhu, *Sci. Rep.*, 2016, **6**, 19347–19355.

31 B. Santara, P. K. Giri, K. Imakita and M. Fujii, *J. Phys. Chem. C*, 2013, **117**, 23402–23411.

32 X. Zhao, Z. Duan and L. Chen, *Ind. Eng. Chem. Res.*, 2019, **58**, 10402–10409.

33 S. Navarro-Jaén, M. Virginie, J. Bonin, M. Robert, R. Wojcieszak and A. Y. Khodakov, *Nat. Rev. Chem.*, 2021, **5**, 564–579.

34 Y. Wang, T. Chen, F. Chen, R. Tang and H. Huang, *Sci. China Mater.*, 2022, **65**, 3497–3503.

35 L. Jiang, Y. Li, X. Wu and G. Zhang, *Sci. China Mater.*, 2021, **64**, 2230–2241.

36 H. Yu, J. Li, Y. Zhang, S. Yang, K. Han, F. Dong, T. Ma and H. Huang, *Angew. Chem., Int. Ed.*, 2019, **58**, 3880–3884.

37 F. Qiu, W. Li, F. Wang, H. Li, X. Liu and C. Ren, *Colloids Surf., A*, 2017, **517**, 25–32.

38 W. Zhao, Q. Zhong, Y. Pan and R. Zhang, *Chem. Eng. J.*, 2013, **228**, 815–823.

39 G. Zhao, J. J. Xu and H. Y. Chen, *Electrochem. Commun.*, 2006, **8**, 148–154.

40 Q. Li, Z. Guan, D. Wu, X. Zhao, S. Bao, B. Tian and J. Zhang, *ACS Sustainable Chem. Eng.*, 2017, **5**, 6958–6968.

41 H. J Stroud, C. E Mohn, J.-A. Hernandez and N. L Allan, *Philos. Trans. R. Soc., A*, 2021, **379**, 2211.

12776 | *J. Mater. Chem. A*, 2023, **11**, 12770–12776

This journal is © The Royal Society of Chemistry 2023